

Coherent Nonlinear Optics and Quantum Control in Negative-Index Metamaterials

A K Popov¹, S A Myslivets² and V M Shalaev³

¹ Department of Physics and Astronomy, University of Wisconsin-Stevens Point, Stevens Point, WI 54481, USA

² Siberian Federal University and Institute of Physics of Russian Academy of Sciences, 660036 Krasnoyarsk, Russian Federation

³ Birk Nanotechnology Center and School of Electrical and Computer Engineering, Purdue University, West Lafayette, IN 47907, USA

E-mail: apopov@uwsp.edu

Abstract. The extraordinary properties of laser-induced transparency of a negative-index slab and parametric amplification for a backward-wave signal are investigated. The effects of the idler absorption and phase mismatch on the amplification of the signal are studied, and the feasibility of ensuring robust transparency for a broad range of control field intensities and slab thicknesses is shown. A particular option consisting of the independent engineering of a strong four-wave mixing response and the negative refractive index is proposed and its specific features are investigated. The feasibility of quantum control over the slab transparency in such a scheme is confirmed through numerical experiments. We thus show opportunities and conditions for the compensation of the strong absorption inherent to plasmonic negative-index metamaterials, and we further show achievable transparency through coherent energy transfer from the control optical field to the negative-index signal.

PACS numbers: 78.67.-n, 42.50.Gy, 42.65.Yj

Keywords: Nonlinear optics, Negative-index metamaterials, Coherent optical effects, Backward waves, Parametric microamplifiers and oscillators

1. Introduction

Negative-index (also known as negative phase velocity or left-handed) metamaterials (NIMs) form a novel class of electromagnetic media that promises revolutionary breakthroughs in photonics [1]. Significant progress has been achieved recently in the design of bulk, multilayered, negative-index, plasmonic structures [2, 3]. The majority of NIMs realized to date consist of metal-dielectric nanostructures that have highly controllable magnetic and dielectric responses. The problem, however, is that these structures have losses that are difficult to avoid, especially in the visible range of frequencies. Irrespective of their origin, losses constitute a major hurdle to the practical realization of the unique optical applications of these structures. Therefore, developing efficient loss-compensating techniques is of paramount importance. So far, the most common approaches to compensating losses in NIMs are related to the investigation of the possibility to embed amplifying centers in the host matrix [1]. The amplification is supposed to be provided through a population inversion between the levels of the embedded centers. Herein, we investigate alternative options based on coherent, nonlinear optical (NLO) energy transfer from the control optical field(s) to the signal through optical parametric amplification (OPA). Nonlinear optics in NIMs remains so far a less-developed branch of optics. On a fundamental level, the NLO response of nanostructured metamaterials is not completely understood or characterized and cannot be predicted effectively to date. Nevertheless, it is well established that local-field enhanced nonlinearities can be attributed to plasmonic nanostructures, and some rough estimates of their magnitude can be obtained. The feasibility of crafting NIMs with strong NLO responses in the optical wavelength range has been experimentally demonstrated in [4]. Unlike natural, positive-index (PI) materials, the energy flow and the phase velocity are counter-directed in NIMs, which determines their extraordinary linear and NLO propagation properties. Unusual properties of nonlinear propagation processes in NIMs, such as second harmonic generation, three-wave mixing (TWM) and four-wave mixing (FWM) OPA, which are in a drastic contrast with their counterparts in natural materials, were shown in [5, 6, 7, 8, 9, 10, 11, 12, 13, 14]. Striking changes in the properties of nonlinear pulse propagation and temporal solitons [15], spatial solitons in systems with bistability [16, 17, 18], gap solitons [19], and optical bistability in layered structures including NIMs [20] were revealed. A review of some of the corresponding theoretical approaches is given in [21].

In the present paper, we investigate the effects of idler absorption and phase mismatch on parametric amplification of the backward waves and propose a novel scheme of compensating losses based on the results of this investigation. The paper is organized as follows. In Section 2, the similarities between the solutions to the nonlinear propagation equations for the electric and magnetic, quadratic and cubic nonlinearities are shown for the case of uniform control fields. Here, the local linear and nonlinear parameters are assumed independent of the intensities of the control fields, and the conclusions are applicable to both TWM and FWM. The induced transparency exhibits a resonance behavior as a function of the control field intensity and the NIM slab's thickness due to the backwardness of the light waves in NIMs. Usually, the resonances are narrow, especially if the parametric process is assisted by amplification of the idler due to Raman or population-inversion gain. The sample remains opaque anywhere beyond the resonance magnitudes of the control field and the resonance thickness of the sample. Counterintuitively, we show that transparency

becomes achievable within a broad range of these parameters if the absorption for the idler exceeds that for the signal. Phase matching of the contrapropagating waves presents a technical challenge [22, 23, 24]. We also show that, in the above indicated case, the transparency of a NIM slab also becomes much more robust against the phase mismatch. Based on these outcomes, we propose and investigate in Section 3 the option of independent engineering of the negative index and FWM nonlinear response, which is different from the one proposed earlier [11, 12, 13]. We consider the doped metamaterial, where the signal appears in the vicinity of the transition between the excited energy levels, whereas the idler couples with the ground state of the embedded quaresonant centers that provide a resonantly enhanced, FWM response. Here, all local optical characteristics including nonlinear susceptibility exhibit a strong dependence on the intensity for the driving fields and on the frequency resonance offsets of the coupled waves. Hence, the output signal can be tailored through the means of quantum control. It is shown that the indicated cardinal changes in the coupling scheme bring about major changes in the properties of the laser-induced transparency of the doped NIM slabs. The possibility of eliminating the negative role of the phase mismatch on the tailored transparency of the slab in this case is also shown. The results, supported by numerical simulations, prove the feasibility of tailored transparency, amplification and the creation of a microscopic, mirrorless, backward-wave, optical parametric oscillator that generates contradirected beams of entangled right- and left-handed photons.

2. Backward waves, parametric interaction in a NIM and solutions to the nonlinear propagation equations

2.1. Poynting and wave-vectors in a lossless NIM

We consider a traveling electromagnetic wave,

$$\mathbf{E}(\mathbf{r}, t) = (1/2)\mathbf{E}_0 \exp[i(\mathbf{k} \cdot \mathbf{r} - \omega t)] + c.c., \quad (1)$$

$$\mathbf{H}(\mathbf{r}, t) = (1/2)\mathbf{H}_0 \exp[i(\mathbf{k} \cdot \mathbf{r} - \omega t)] + c.c. \quad (2)$$

From the equations

$$\nabla \times \mathbf{E} = -\frac{1}{c} \frac{\partial \mathbf{B}}{\partial t}, \mathbf{B} = \mu \mathbf{H}, \nabla \times \mathbf{H} = \frac{1}{c} \frac{\partial \mathbf{D}}{\partial t}, \mathbf{D} = \epsilon \mathbf{E} \quad (3)$$

one finds that

$$\mathbf{k} \times \mathbf{E} = \frac{\omega}{c} \mu \mathbf{H}, \mathbf{k} \times \mathbf{H} = -\frac{\omega}{c} \epsilon \mathbf{E}, \sqrt{\epsilon} E = -\sqrt{\mu} H. \quad (4)$$

Equations (4) show that the vector triplet \mathbf{E} , \mathbf{H} , \mathbf{k} forms a right-handed system for an ordinary medium with $\epsilon_i > 0$ and $\mu_i > 0$. Simultaneously negative ϵ_i and μ_i result in a left-handed triplet and negative refractive index

$$n = -\sqrt{\mu\epsilon}, \quad k^2 = n^2(\omega/c)^2. \quad (5)$$

We assume here that all indices of ϵ , μ and n are real numbers. The direction of the wave-vector \mathbf{k} with respect to the energy flow (Poynting vector) depends on the signs of ϵ and μ :

$$\mathbf{S}(\mathbf{r}, t) = \frac{c}{4\pi} [\mathbf{E} \times \mathbf{H}] = \frac{c^2 \mathbf{k}}{4\pi\omega\epsilon} H^2 = \frac{c^2 \mathbf{k}}{4\pi\omega\mu} E^2. \quad (6)$$

At $\epsilon_i < 0$ and $\mu_i < 0$, \mathbf{S} and \mathbf{k} become contradirected, which is in contrast with the electrodynamics of ordinary media and opens opportunities for many revolutionary breakthroughs.

2.2. Coupling geometry and coherent energy transfer from the ordinary control fields to the backward signal in a NIM

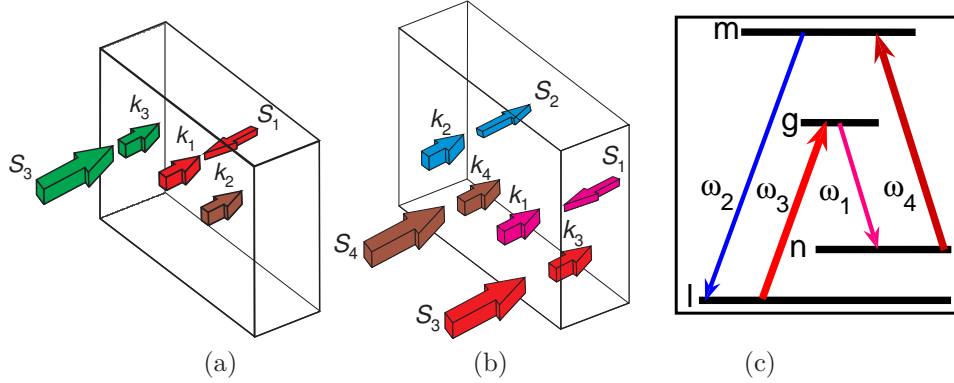


Figure 1. Coupling geometry for three-wave mixing (a), four-wave mixing (b) of the ordinary and one backward electromagnetic waves and scheme of quantum controlled four-wave mixing in the embedded resonant nonlinear-optical centers (c). Here, \mathbf{S}_1 , \mathbf{k}_1 and ω_1 are energy flow, wave-vector and frequency of the negative-index signal ($n_1 < 1$); $\mathbf{S}_{3,4}$, $\mathbf{k}_{3,4}$ and $\omega_{3,4}$ - of the positive-index control fields; \mathbf{k}_2 and ω_2 stand for the positive-index idler.

The basic idea of compensating losses by coherent energy transfer from the control field(s) to the signal through parametric interaction is illustrated in Fig. 1. We assume the wave at ω_1 with the wave-vector \mathbf{k}_1 directed along the z -axis is a negative-index (NI) ($n_1 < 0$) signal. Therefore, it is a backward wave because its energy flow $\mathbf{S}_1 = (c/4\pi)[\mathbf{E}_1 \times \mathbf{H}_1]$ appears directed against the z -axis. In the TWM case, shown in Fig. 1(a), the medium is illuminated by a higher-frequency, ordinary PI wave at ω_3 traveling along the z -axis ($n_3 > 0$). In the FWM case, Fig. 1(b), the slab is illuminated by two PI control (pump) waves at ω_3 and ω_4 . In both cases, all wave-vectors are co-directed along the z -axis. Due to the parametric interaction, the control and signal fields generate a difference-frequency idler at $\omega_2 = \omega_3 - \omega_1$ (TWM) or at $\omega_2 = \omega_4 + \omega_3 - \omega_1$ (FWM), which is also assumed to be a PI wave ($n_2 > 0$). The idler contributes back into the wave at ω_1 through the same type of the parametric interaction and thus enables OPA at ω_1 by converting the energy of the control fields into the signal. Thus, all of the coupled waves have their wave-vectors co-directed along z , whereas the energy flow of the signal wave, \mathbf{S}_1 , is counter-directed to the energy flows of all the other waves, which are codirected with their wave-vectors. Such coupling schemes are in contrast both with the conventional phase-matching scheme for OPA in ordinary materials, where all energy-flows and phase velocities are co-directed, as well as with TWM backward-wave mirrorless OPO [22, 23, 24, 25], where both the energy flow and wave-vector of one of the waves are opposite to all others.

2.3. Equations for coupled contrapropagating backward and ordinary waves

First, we shall show that magnetic and electric TWM and FWM processes can be treated identically. We consider two alternative types of nonlinearities – electric,

$\mathbf{D} = \epsilon\mathbf{E} + 4\pi\mathbf{P}^{NL}$, $\mathbf{B} = \mu\mathbf{H}$; and magnetic, $\mathbf{B} = \mu\mathbf{H} + 4\pi\mathbf{M}^{NL}$, $\mathbf{D} = \epsilon\mathbf{E}$. Nonlinear polarization and magnetization are sought in the form

$$\mathbf{P}^{NL}(\mathbf{r}, t) = (1/2)\mathbf{P}_0^{NL}(\mathbf{r}) \exp[i(\tilde{\mathbf{k}} \cdot \mathbf{r} - \omega t)] + c.c., \quad (7)$$

$$\mathbf{M}^{NL}(\mathbf{r}, t) = (1/2)\mathbf{M}_0^{NL}(\mathbf{r}) \exp[i(\tilde{\mathbf{k}} \cdot \mathbf{r} - \omega t)] + c.c. \quad (8)$$

Accounting for Eqs. (4), one can derive

$$\begin{aligned} \nabla \times \nabla \times \mathbf{E} &= -(\mu/c^2)\partial^2\mathbf{D}/\partial t^2, \\ -\Delta\mathbf{E} &= \mu(\omega^2/c^2)[\epsilon\mathbf{E} + 4\pi\mathbf{P}^{NL}], \end{aligned} \quad (9)$$

$$\begin{aligned} \nabla \times \nabla \times \mathbf{H} &= -(\epsilon/c^2)\partial^2\mathbf{B}/\partial t^2, \\ -\Delta\mathbf{H} &= \epsilon(\omega^2/c^2)[\mu\mathbf{H} + 4\pi\mathbf{M}^{NL}]. \end{aligned} \quad (10)$$

For the medium with the electric nonlinearity, the equation for the slowly varying amplitude \mathbf{E}_0 of the wave with the wave-vector along the z -axis takes the form:

$$dE_0/dz = i\mu(2\pi\omega^2/kc^2)P_0^{NL} \exp[i(\tilde{k} - k)z]. \quad (11)$$

For the magnetic nonlinearity, the equation is

$$dH_0/dz = i\epsilon(2\pi\omega^2/kc^2)M_0^{NL} \exp[i(\tilde{k} - k)z]. \quad (12)$$

The equations are symmetric and can be converted from one to the other by replacing $\mu \longleftrightarrow \epsilon$.

For the electric quadratic nonlinearity,

$$P_1^{NL} = \chi_{e1}^{(2)} E_3 E_2^* \exp\{i[(k_3 - k_2)z - \omega_1 t]\}, \quad (13)$$

$$P_2^{NL} = \chi_{e2}^{(2)} E_3 E_1^* \exp\{i[(k_3 - k_1)z - \omega_2 t]\}, \quad (14)$$

where $\omega_2 = \omega_3 - \omega_1$ and $k_j = |n_j|\omega_j/c > 0$. Then the equations for the slowly-varying amplitudes of the signal and idler in the lossy medium can be given in the form

$$dE_1/dz = i\sigma_{e1}E_2^* \exp[i\Delta kz] + (\alpha_1/2)E_1, \quad (15)$$

$$dE_2/dz = i\sigma_{e2}E_1^* \exp[i\Delta kz] - (\alpha_2/2)E_2. \quad (16)$$

Here, $\sigma_{ej} = (k_j/\epsilon_j)2\pi\chi_{ej}^{(2)}E_3$, $\Delta k = k_3 - k_2 - k_1$, and α_j are the absorption indices. The amplitude of the control (pump) wave E_3 is assumed constant.

For the magnetic type of quadratic nonlinearity,

$$M_1^{NL} = \chi_{m1}^{(2)} H_3 H_2^* \exp\{i[(k_3 - k_2)z - \omega_1 t]\}, \quad (17)$$

$$M_2^{NL} = \chi_{m2}^{(2)} H_3 H_1^* \exp\{i[(k_3 - k_1)z - \omega_2 t]\}, \quad (18)$$

the equations for the slowly-varying amplitudes are:

$$dH_1/dz = i\sigma_{m1}H_2^* \exp[i\Delta kz] + (\alpha_1/2)H_1, \quad (19)$$

$$dH_2/dz = i\sigma_{m2}H_1^* \exp[i\Delta kz] - (\alpha_2/2)H_2. \quad (20)$$

Here, $\sigma_{mj} = (k_j/\mu_j)2\pi\chi_{mj}^{(2)}H_3$, $H_3 = \text{const}$, and the other notations remain the same.

For the electric-type FWM, the equations for the slowly-varying amplitudes are similar:

$$dE_1/dz = i\gamma_1 E_2^* \exp[i\Delta kz] + (\alpha_1/2)E_1, \quad (21)$$

$$dE_2/dz = i\gamma_2 E_1^* \exp[i\Delta kz] - (\alpha_2/2)E_2. \quad (22)$$

Here, $\gamma_j = (k_j/\epsilon_j)2\pi\chi_j^{(3)}E_3E_4$ and $\Delta k = k_3 + k_4 - k_1 - k_2$.

We note the following three fundamental differences in equations (15)-(22) as compared with their counterpart in ordinary, PI materials. First, the signs of σ_1 and

γ_1 are opposite to those of σ_2 and γ_2 because $\epsilon_1 < 0$ and $\mu_1 < 0$. Second, the opposite sign appears with α_1 because the energy flow \mathbf{S}_1 is against the z -axis. Third, the boundary conditions for the signal are defined at the opposite side of the sample as compared to the idler because the energy flows \mathbf{S}_1 and \mathbf{S}_2 are counter-directed.

We introduce effective amplitudes, $a_{e,m,j}$, and nonlinear coupling parameters, $g_{e,m,j}$, which for the electric and magnetic types of quadratic nonlinearity are defined as

$$a_{ej} = \sqrt{|\epsilon_j/k_j|} E_j, g_{ej} = \sqrt{|k_1 k_2 / \epsilon_1 \epsilon_2|} 2\pi \chi_{ej}^{(2)} E_3, \quad (23)$$

$$a_{mj} = \sqrt{|\mu_j/k_j|} H_j, g_{mj} = \sqrt{|k_1 k_2 / \mu_1 \mu_2|} 2\pi \chi_{mj}^{(2)} H_3, \quad (24)$$

and for FWM as

$$a_j = \sqrt{|\epsilon_j/k_j|} E_j, g_j = \sqrt{|k_1 k_2 / \epsilon_1 \epsilon_2|} 2\pi \chi_j^{(3)} E_3 E_4. \quad (25)$$

The quantities $|a_j|^2$ are proportional to the photon numbers in the energy fluxes. Equations for amplitudes a_j are identical for all of the types of nonlinearities studied here:

$$da_1/dz = -g_1 a_2^* \exp(i\Delta k z) + (\alpha_1/2) a_1, \quad (26)$$

$$da_2/dz = g_2 a_1^* \exp(i\Delta k z) - (\alpha_2/2) a_2. \quad (27)$$

2.4. Manley-Rowe relations and solutions to the equations for coupled counter-propagating waves

At $\alpha_{1,2} = 0$, $g_1 = g_2$, e.g., for off-resonant coupling, one finds with the aid of equations (6) and (26), (27):

$$\frac{d}{dz} \left[\frac{S_{1z}}{\hbar\omega_1} - \frac{S_{2z}}{\hbar\omega_2} \right] = 0, \quad \frac{d}{dz} [|a_1|^2 + |a_2|^2] = 0. \quad (28)$$

These equations represent the Manley-Rowe relations [26], which describe the creation of pairs of entangled counter-propagating photons $\hbar\omega_1$ and $\hbar\omega_2$. The second equation predicts that the sum of the terms proportional to the squared amplitudes of the signal and idler remains constant through the sample, which is due to the opposite signs of S_{1z} and S_{2z} and is in contrast with the requirement that the difference of such terms is constant in the analogous case in ordinary nonlinear-optical materials.

Taking into account the boundary conditions $a_1(z=L) = a_{1L}$, and $a_2(z=0) = a_{20}$ (L is the slab thickness), the solutions to equations (26), (27) can be written as

$$\begin{aligned} a_1(z) &= A_1 \exp[(\beta_1 + i\frac{\Delta k}{2})z] + \\ &+ A_2 \exp[(\beta_2 + i\frac{\Delta k}{2})z], \end{aligned} \quad (29)$$

$$\begin{aligned} a_2^*(z) &= \kappa_1 A_1 \exp[(\beta_1 - i\frac{\Delta k}{2})z] + \\ &+ \kappa_2 A_2 \exp[(\beta_2 - i\frac{\Delta k}{2})z], \end{aligned} \quad (30)$$

where

$$\beta_{1,2} = (\alpha_1 - \alpha_2)/4 \pm iR, \quad \kappa_{1,2} = [\pm R + is]/g, \quad (31)$$

$$R = \sqrt{g^2 - s^2}, \quad g^2 = g_2^* g_1, \quad s = (\alpha_1 + \alpha_2)/4 - i\Delta k/2, \quad (32)$$

$$A_1 = \{a_{1L}\kappa_2 - a_{20}^* \exp[(\beta_2 + i\frac{\Delta k}{2})L]\}/D, \quad (33)$$

$$A_2 = -\{a_{1L}\kappa_1 - a_{20}^* \exp[(\beta_1 + i\frac{\Delta k}{2})L]\}/D, \quad (34)$$

$$D = \kappa_2 \exp[(\beta_1 + i\frac{\Delta k}{2})L] - \kappa_1 \exp[(\beta_2 + i\frac{\Delta k}{2})L]. \quad (35)$$

At $\Delta k = 0$ and $\text{Im } g = 0$, $(\alpha_1 + \alpha_2)L \ll \pi$ (off-resonance), equations (29) and (30) reduce to

$$a_1^*(z) \approx \frac{a_{1L}^*}{\cos(gL)} \cos(gz) + \frac{ia_{20}}{\cos(gL)} \sin[g(z - L)], \quad (36)$$

$$a_2(z) \approx \frac{ia_{1L}^*}{\cos(gL)} \sin(gz) + \frac{a_{20}}{\cos(gL)} \cos[g(z - L)]. \quad (37)$$

The output amplitudes are then given by

$$a_{10}^* = [a_{1L}^*/\cos(gL)] - ia_{20} \tan(gL), \quad (38)$$

$$a_{2L} = ia_{1L}^* \tan(gL) + [a_{20}/\cos(gL)]. \quad (39)$$

At $a_{20} = 0$, the equations for the energy distribution for the backward wave, $T_1(z) = |a_1(z)/a_{1L}|^2$, and for the PI idler, $\eta_2(z) = |a_2(z)/a_{1L}^*|^2$, across the slab take the form

$$T_1(z) = |[\kappa_2 \exp(\beta_1 z) - \kappa_1 \exp(\beta_2 z)]/D|^2, \quad (40)$$

$$\eta_2(z) = |[\exp(\beta_1 z) - \exp(\beta_2 z)]/D|^2. \quad (41)$$

Then the transmission factor for the backward-wave signal at $z = 0$, T_{10} , and the output idler at $z = L$, η_{2L} , are given by

$$T_{10} = \left| \frac{a_1(0)}{a_{1L}} \right|^2 = \left| \frac{\exp\{ - [(\alpha_1/2) - s] L \}}{\cos RL + (s/R) \sin RL} \right|^2, \quad (42)$$

$$\eta_{2L} = \left| \frac{a_2(L)}{a_{1L}} \right|^2 = \left| \frac{(g/R) \sin RL}{\cos RL + (s/R) \sin RL} \right|^2. \quad (43)$$

At $a_{1L} = 0$, $a_2(z = 0) = a_{20}$, the slab serves as an NLO mirror with a reflectivity (output conversion efficiency) at ω_1 given by an equation identical to Eq.(43):

$$\eta_{10} = \left| \frac{a_1(0)}{a_{20}^*} \right|^2 = \left| \frac{(g/R) \sin RL}{\cos RL + (s/R) \sin RL} \right|^2. \quad (44)$$

3. Laser-induced transparency, amplification and generation of the backward wave

The fundamental difference between the spatial distribution of the signal in ordinary and NI slabs is explicitly seen at $\alpha_j = \Delta k = 0$. There, equation (42) reduces to

$$T_{10} = 1/[\cos(gL)]^2. \quad (45)$$

Equations (36)-(45) show that the output signal and idler experience a sequence of geometrical resonances at $gL \rightarrow (2j + 1)\pi/2$, ($j=0, 1, 2, \dots$), as functions of the slab thickness L and of the intensity of the control field (factor g). Such behavior is in drastic contrast with that in an ordinary medium, where the signal would grow exponentially as $T_1 \propto \exp(2gL)$. The resonances indicate that strong absorption of the left-handed wave and of the idler can be turned into transparency, amplification

and even into cavity-free self-oscillation when the denominator tends to zero. The conversion factors η_{10} and η_{20} experience a similar resonance increase. Self-oscillations would provide for the generation of entangled counter-propagating left-handed, $\hbar\omega_1$, and right-handed, $\hbar\omega_2$, photons without a cavity. A similar behavior is characteristic for distributed-feedback lasers and is equivalent to a great extension of the NLO coupling length. It is known that even weak amplification per unit length may lead to lasing provided that the corresponding frequency coincides with high-quality cavity or feedback resonances. Below, we present investigation of the properties of such resonances.

3.1. Effect of the idler absorption and phase mismatch on the laser-induced transparency resonances

In order to demonstrate the major effects of the idler absorption and phase mismatch on the laser-induced transparency resonances, we consider the model where the dependence of the local optical and NLO parameters on the intensity of the control field can be neglected and the parameter g is real. Such a model is relevant to, e.g., off-resonant quadratic and cubic nonlinearities attributed to the structural elements of metal-dielectric nanocomposites [4]. The results will be used in the next subsection for optimization of the transparency achievable through embedded resonant FWM centers with power-dependent optical parameters. A crucial role of the outlined geometrical resonances is illustrated in Figs. 2 and 3. Besides the factor g , the local NLO energy conversion rate for each of the waves is proportional to the amplitude of another coupled wave and depends on the phase mismatch Δk . Hence, the fact that the waves decay in opposite directions causes a specific, strong dependence of the entire propagation process and, consequently, of the transmission properties of the slab on the ratio of the decay rates [14]. A typical NIM slab absorbs about 90% of light at the frequencies which are in the NI frequency range. Such absorption corresponds to $\alpha_1 L \approx 2.3$. Since the idler grows toward the back facet of the slab and the signal experiences absorption in the opposite direction, the maximum of the signal for the given parameters is located closer to the back facet of the slab. A change in the slab thickness or in the intensity of the control fields leads to significant changes in the distributions of the signal and idler along the slab and in their output values (Fig. 2). As outlined above, the transparency exhibits an extraordinary resonance behavior as a function of the intensity of the control field and the NIM slab thickness, which occurs due to the backwardness of the light waves in NIMs and is illustrated in Fig. 3. Basically, such resonances are narrow, like those depicted in the plot corresponding to $\alpha_2 L = 1$ in Fig. 3(a), and the sample remains opaque anywhere beyond the resonance field and the parameters of the sample. If nonlinear susceptibility varies within the negative-index frequency domain, this translates into relatively narrow-band filtering. The slab would become transparent within the broad range of the slab thickness and the control field intensity if the transmission in all of the minimums is about or more than 1. Figure 3 shows the feasibility of achieving robust transparency and amplification in a NIM slab at the signal frequency through a wide range of the control field intensities and slab thicknesses by the appropriate adjustment of the absorption indices $\alpha_2 \geq \alpha_1$. Figure 3(a) depicts transmission properties of the NIM slab at $\alpha_1 L = 2.3$ and different magnitudes of the absorption index $\alpha_2 L > 0$ that are less than, equal to and greater than $\alpha_1 L$. The figure shows dramatic changes in the transmission properties with changes in the ratio of the absorption indices

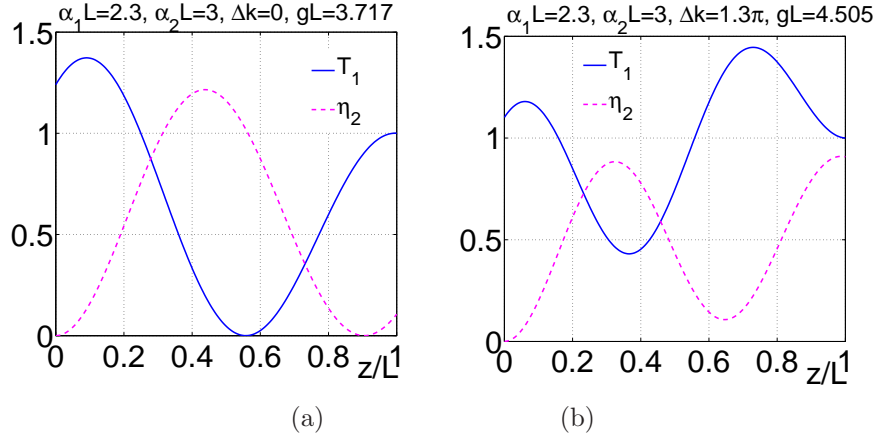


Figure 2. Tailored distribution of the signal, $T_1(z) = |a_1(z)/a_1(L)|^2$, and of the idler, $\eta_2(z) = |a_2(z)/a_1(L)|^2$, along the slab at $\alpha_1 L = 2.3$, $\alpha_2 L = 3$ in the first transmission minimum. (a): $\Delta k = 0$, $gL = 3, 717$. (b): $\Delta k = 1.3\pi$, $gL = 4, 505$.

for the signal, α_1 , and the idler, α_2 . It is seen that the transmissions does not drop below 1 at $\alpha_2 > \alpha_1$. Hence, larger absorption for the idler is advantageous for robust transmission of the signal, which is counterintuitive. The increase of the idler's absorption is followed by the relatively small shift of the resonances to larger magnitudes of gL . Oscillation amplitudes grow sharply near the resonances, which indicates cavity-less generation. The distribution of the signal and the idler inside the slab would also dramatically change, as compared to that for the first transmission minimum depicted in Fig. 2. Unless optimized, the signal maximum inside the slab may appear much greater than its output value at $z = 0$. Phase-matching of the positive- and negative-index waves also presents a technical challenge. Figures 3(b)-(d) show the possibility to significantly diminish the negative role of the phase mismatch on the tailored transparency of the slab at the expense of a modest increase of the amplitude of the control field. At that, the spatial distribution of the signal and the idler may experience a dramatic change [Fig. 2 (b)]. Such dependencies are in strong contrast with their counterparts in PI materials and are determined by the backwardness of the coupled waves that is inherent to NIMs.

Only rough estimations can be made regarding $\chi^{(2)}$ attributed to metal-dielectric nanostructures. Assuming $\chi^{(2)} \sim 10^{-6}$ ESU ($\sim 10^3$ pm/V), which is on the order of that for CdGeAs₂ crystals, and a control field of $I \sim 100$ kW focused on a spot of $D \sim 50 \mu\text{m}$ in diameter, one can estimate that the typical threshold value of $gL \sim 1$ can be achieved for a slab thickness in the microscopic range of $L \sim 1 \mu\text{m}$, which is comparable with that of the multilayer NIM samples fabricated to date [3, 2].

3.2. Independent engineering of NLO response, quasi-resonant four-wave mixing of ordinary and backward waves and quantum control of transparency of NIM slab

Herein, we explore the feasibility of independently engineering the NI and the resonantly enhanced $\chi^{(3)}$ -response of a composite metamaterial with embedded NLO centers. We investigate resonant and quasi-resonant FWM and the accompanying processes that allow coherent energy transfer from the control fields to the counter-

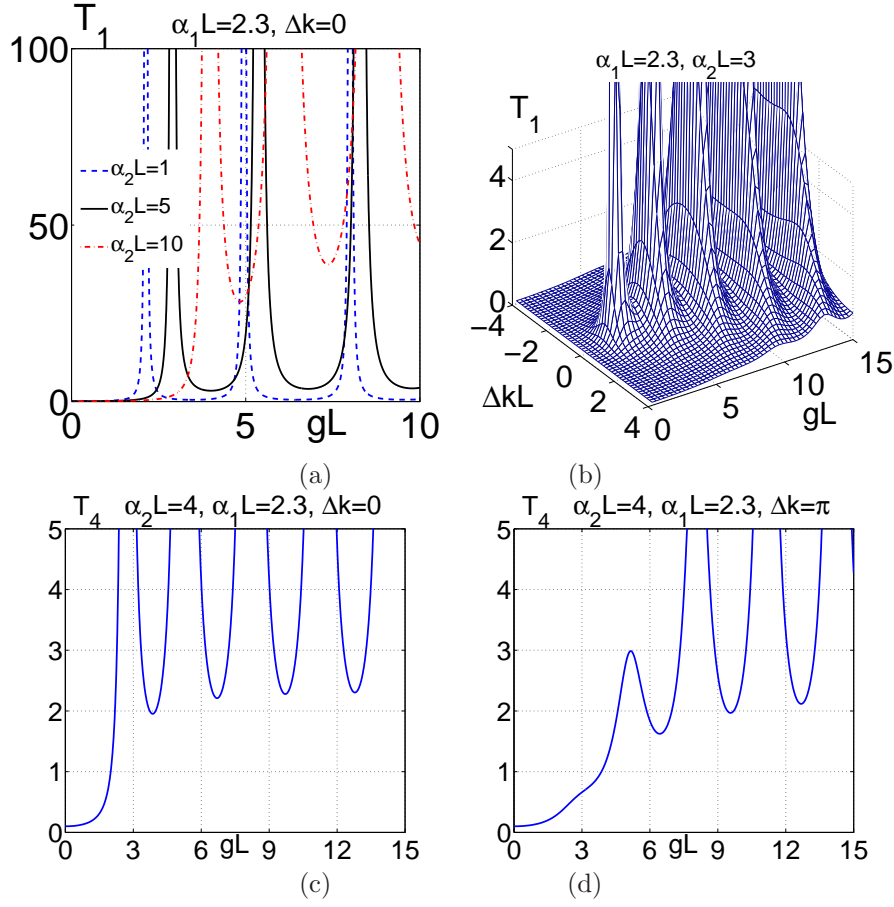


Figure 3. Transmission of the negative-index slab, $T_1(z)$, vs. parametric gain, gL , at $\alpha_1 L = 2.3$ and different values of $\alpha_2 L$ and $\Delta k L$. [(a), (c)] $\Delta k = 0$; [(d)] $\Delta k = \pi$; [(c), (d)] $\alpha_2 L = 4$.

propagating NI signal and PI idler. We show that this opens up opportunities for compensating optical losses in NIMs and for the creation of unique NIM-based photonic microdevices, which are of critical importance for the further development of nanophotonics in NIMs (for a review, see, for example, [1]). Among the specific features considered in this study are the above-outlined backwardness of the coupled waves and the possibility of quantum control over the nonlinear propagation process and its outcomes. The basic scheme of resonant four-wave mixing of the backward wave in a NIM is as follows. A slab of NIM is doped by four-level nonlinear centers [Fig. 1(c)] so that the signal frequency, ω_1 , falls in the NI domain, whereas all other frequencies, ω_3 , ω_4 and ω_2 , are in the the PI domain. Below, we show the possibility to produce transparency and even amplification above the oscillation threshold at ω_1 controlled by two lasers at ω_3 and ω_4 [Fig. 1(b)]. These fields generate an idler at $\omega_2 = \omega_3 + \omega_4 - \omega_1$, which then contributes back in optical parametric amplification at ω_1 . Unlike the scheme investigated in [11, 12, 13], here the idler corresponds to a higher-frequency transition from the ground state, and the signal

corresponds to a lower-frequency transition between the excited states. No incoherent amplification is possible here for the idler, and the dependence of the idler and the signal absorption indices on the control fields cardinally changes. First, the scheme with relatively fast quantum coherence relaxation rates and the case where only a two-photon, Raman-like resonance for the signal holds is considered; all other one-photon frequency offsets are on the order of several tens of the optical transition widths. Then the scheme with the same quantum coherence relaxation rates but with higher partial spontaneous transition rates is considered, in which case population inversion at the coupled optical transitions is impossible. Finally we consider the scheme with longer quantum coherence lifetimes, which still does not allow population inversion at the optical transitions nor Raman-like amplification. The fact that all involved optical transitions are absorptive determines essentially different features of the overall loss-compensation technique in such composites in each proposed scheme. In all of the schemes outlined above, the linear and nonlinear local parameters can be tailored through quantum control by varying the intensities and frequency-resonance offsets for combinations of the two control driving fields.

The following model, which is characteristic of ions and some molecules embedded in a solid host, has been adopted: energy level relaxation rates $\Gamma_n = 20$, $\Gamma_g = \Gamma_m = 120$; partial transition probabilities $\gamma_{gn} = 50$, $\gamma_{mn} = 70$, (all in 10^6 s^{-1}); homogeneous transition half-widths $\Gamma_{lg} = 1$, $\Gamma_{lm} = 1.9$, $\Gamma_{ng} = 1.5$, $\Gamma_{nm} = 1.8$ (all in 10^{12} s^{-1}); $\Gamma_{gm} = 5$, $\Gamma_{ln} = 1$ (all in 10^{10} s^{-1}); $\lambda_1 = 756 \text{ nm}$ and $\lambda_2 = 480 \text{ nm}$. The density-matrix method [28] is used for calculating the intensity-dependent local parameters while accounting for the quantum nonlinear interference effects. This allows us to investigate the changes in absorption, amplification, and refractive indices as well as in the magnitudes and signs of NLO susceptibilities caused by the control fields. These changes depend on the population redistribution over the coupled levels, which in turn strongly depends on the ratio of the partial transition probabilities. Electrical linear and nonlinear polarizations, Eq. (7), are calculated as

$$\begin{aligned} P_1(z, t) &= (1/2)\{P_{01}^L \exp(ik_1 z) \\ &+ P_{01}^{NL} \exp[i(k_3 + k_4 - k_2)z]\} \exp(-i\omega_1 t) + c.c. \\ &= N(\rho_{ng}d_{gn} + \rho_{gn}d_{ng}); \end{aligned} \quad (46)$$

$$\begin{aligned} P_2(z, t) &= (1/2)\{P_{02}^L \exp(ik_2 z) \\ &+ P_{02}^{NL} \exp[i(k_3 + k_4 - k_1)z]\} \exp(-i\omega_2 t) + c.c. \\ &= N(\rho_{ml}d_{lm} + \rho_{lm}d_{ml}). \end{aligned} \quad (47)$$

Here, ρ_{ij} are the density matrix elements, and d_{ij} are the transition dipole elements. Effective linear, $\chi_{1,2}$, and NLO, $\chi_{1,2}^{(3)}$, susceptibilities dependent on the intensities of the driving control fields E_3 and E_2 are defined as

$$P_{01}^L = \chi_1 E_1, \quad P_{01}^{NL} = \chi_1^{(3)} E_3 E_4 E_2^*; \quad (48)$$

$$P_{02}^L = \chi_2 E_2, \quad P_{02}^{NL} = \chi_2^{(3)} E_3 E_4 E_1^*. \quad (49)$$

The linear susceptibilities determine the intensity-dependent contributions to absorption and to the refractive indices of the composite attributed to the embedded centers, while the NLO susceptibilities determine the FWM. Here, $\omega_1 + \omega_2 = \omega_3 + \omega_4$, and $k_j = |n_j|\omega_j/c > 0$. A significant difference between the resonant and off-resonant NLO processes is that all local optical parameters become intensity-dependent, and hence their spectral properties may experience a radical change near resonance. In particular, the NLO susceptibilities and, therefore, the parameters γ_1 and γ_2 become complex and differ from each other in the vicinity of the resonances. Hence, the factor

g^2 may become negative or complex. This indicates an additional phase shift between the NLO polarization and the generated wave that causes further radical changes in the nonlinear propagation features, which can be tailored.

Figure 4 depicts such modifications at the given resonance offsets and intensities of the control fields. Here, $\Omega_1 = \omega_1 - \omega_{gn}$; other resonance detunings Ω_j are defined in a similar way. Coupling Rabi frequencies are introduced as $G_3 = E_3 d_{lg}/2\hbar$ and $G_4 = E_4 d_{nm}/2\hbar$. The quantity α_{20} denotes the fully resonant value of absorption introduced by the embedded centers at $\omega_2 = \omega_{ml}$ with all driving fields turned off. Figure 4(a) displays the modified absorption/gain indices. The nonlinear spectral structures are caused by the modulation of the probability amplitudes, which exhibits itself as an effective splitting of the energy levels coupled with the driving fields. Figure 4(b) shows the contribution to the phase mismatch associated with one such spectral structure. Figure 4(c) and (d) indicate that the real and imaginary parts of the NLO susceptibilities become commensurate for the given susceptibility, but may exceed their counterparts for the idler by several times. This occurs due to the fact that different population differences contribute in different ways to the NLO susceptibilities [28], and driving fields cause significant redistributions of the level populations (Fig. 5). At the given partial probabilities of spontaneous transition between the levels, population inversions at the signal transition become possible [Fig.5(e),(g)-(i)]. However, for the given frequency offsets of the control fields, corresponding amplification contributes negligibly to the energy conversion [Fig.4(a)]. Alternatively, two-photon, Raman-like amplification at $\Omega_1 \approx 20.05\Gamma_{gn}$ shown in Fig.4(a) supports coherent, parametric energy-conversion from the control fields to the signal. Figures 6(a)-(d) display the spectral properties of the output signal at $z = 0$ for one of the resonances in the vicinity of the signal frequency offset $\omega_1 - \omega_{gn} \approx 20.05\Gamma_{gn}$ at different optical densities of the slab at ω_{ml} attributed to the impurity centers. We assume that the absorption of the host material in the slab at ω_1 is fixed at 90% and it is equal to 88% at ω_2 . The density of the embedded centers and the slab thickness, and hence, the additional resonant optical thickness of the slab contributed by these impurities, may vary as shown in the panels. Actual quasi-resonant absorption/gain indices depend on the intensities and frequency offsets of the control fields, as shown in Fig.4(a). Besides the features imposed by the counter-propagation of the coupled waves, the output magnitudes of the signal at $z = 0$ and the idler at $z = L$ and their distributions inside the slab are determined by the interplay of several contributing linear and nonlinear processes. They include the phase mismatch, absorption of the signal and the idler, and the parametric gain g , which are all controlled by the driving fields E_3 and E_4 . The dependence of the overall optimized output signal on the density of the impurities and on the slab thickness (on the resonant optical thickness of the slab) is depicted in Fig. 6(e). Such a behavior is determined by the radically different distributions of the idler, which propagates from left to right, and the signal, which propagates from right to left, [Fig. 6(f)]. Figures 6(b)-(f) indicate the possibility of mirrorless self-oscillation. Figure 7 shows the role of partial spontaneous transitions between the energy levels. Here, $\gamma_{mn} = 9 \times 10^7 \text{ sec}^{-1}$, which makes both population inversion and two-photon gain impossible [Fig. 7(a)]. At the indicated Rabi frequencies and frequency offsets for the driving control fields, the energy-level populations are: $r_l \approx 0.4$, $r_g \approx 0.2009$, $r_n \approx 0.2031$, $r_m \approx 0.2$. The magnitude of the four-wave mixing coupling parameters appear comparable with those depicted in Fig. 4(c)-(h). However, the absence of one- and two-photon amplification that would support energy-conversion processes, like in

[12] and in Fig. 4(a), dramatically decreases the achievable amplification and increases the required optical thickness of the slab [Fig. 7(g),(h)]. Figure 8 shows that, even in such cases, the optimized magnitude of the required control field intensities and the slab optical density can be substantially reduced for centers with lower coherence relaxation rates and quasi-resonant coupling. Here, quantum nonlinear interference effects play an important role [28]. At the indicated Rabi frequencies and frequency offsets for the driving control fields shown in Fig. 8, the energy-level populations are: $r_l \approx 0.504$, $r_g \approx 0.165$, $r_n \approx 0.167$, $r_m \approx 0.164$. Like in the previous examples, the losses in the host NIM material are taken to be fixed and equal to $\alpha_{NIM1}L = 2.3$ for the signal and $\alpha_{NIM2}L = 2.1$ for the idler.

The dependencies presented in Figs. 4 - 8 correspond to the vicinity of the first geometrical resonance, which appears at the lowest magnitude of gL as shown in Fig. 3. For the above-indicated characteristics of the involved optical transitions, the magnitude $G=150$ GHz corresponds to control field intensities on the order of $I \sim 10$ kW/(0.1mm)². Assuming a resonance absorption cross-section $\sigma_{40} \sim 10^{-16}$ cm², which is typical for transitions with oscillator strength of about one, and a concentration of embedded centers $N \sim 10^{19}$ cm⁻³, we obtain $\alpha_{20} \sim 10^3$ cm⁻¹ and the required slab thickness in the microscopic range $L \sim (1 - 100)\mu\text{m}$. The contribution to the index of refraction by the impurities is estimated as $\Delta n < 0.5(\lambda/4\pi)\alpha_{40} \sim 10^{-3}$, which essentially does not change the negative refractive index.

4. Conclusions

The possibility to produce and to tailor a laser-induced optical transparency in a negative-index metamaterial slab through nonlinear-optical coherent energy transfer between ordinary control wave(s) and a negative-index backward signal is shown and proven by numerical simulations. Two possible types of nonlinear-optical couplings are discussed. One is off-resonant three or four-wave mixing by making use of the nonlinear susceptibilities that are assumed attributed to the metamaterial nanostructures and are independent of the intensities and frequencies of the coupled optical fields. The other option is the independent engineering of a resonantly enhanced, four-wave mixing nonlinearity associated with nonlinear-optical centers embedded in a negative-index host matrix. In the latter case, the proposed coupling scheme suggests that the frequency of the negative-index signal should fall in the vicinity of the transition between the excited levels of the centers, while the idler frequency appears coupled with the absorptive transition from the ground state. The scheme under investigation is different from the earlier proposed schemes and exhibits essentially different features. The extraordinary properties of the nonlinear-optical propagation processes in both outlined types of metamaterials are investigated. These properties are in drastic contrast with their counterparts in ordinary, positive index materials. The focus of this work is on the possibility of compensating for the strong losses inherent to metal-dielectric negative-index metamaterials and on producing laser-induced optical transparency and gain for the negative-index signal. In the case of a frequency- and intensity-independent nonlinear-optical response of the composite, the feasibility of producing transparency and amplification through the entire negative-index frequency domain above a certain control laser field intensity is investigated. This is shown to be possible by adjusting the absorption index for the idler to be greater than that for the negative-index signal. Specific features of the quantum control attributed to the

second scheme are investigated that allow for transformable optics through frequency-tunable narrow-band transparency, quantum switching, filtering and amplification of light. The possibility of compensating the strong losses inherent to NIMs and realizing a miniature, mirrorless optical parametric generator of entangled contra-propagating backward and ordinary waves is also shown and supported by numerical simulations. The extraordinary features predicted in this work stem from the backwardness of electromagnetic waves, which is a feature inherent to this type of metamaterial.

Acknowledgment

This work was supported by the U. S. Army Research Laboratory and by the U. S. Army Research Office under grants number W911NF-0710261 and 50342-PH-MUR and by the Siberian Division of the Russian Academy of Sciences under Integration Project No 5.

References

- [1] V. M. Shalaev, "Optical negative-index metamaterials," *Nat. Photonics* **1**, 41-48 (2007).
- [2] Costas M. Soukoulis and Maria Kafesaki, "Weakly and strongly coupled optical metamaterials," Invited talk at the Nanometa 2009, The 2nd European Topical Meeting on Nanophotonics and Metamaterials 5 - 8 January, 2009, Seefeld, Tirol, Austria; N. Katsarakis, G. Konstantinidis, A. Kostopoulos, R. S. Penciu, T. F. Gundogdu, M. Kafesaki, E. N. Economou, Th. Koschny, and C. M. Soukoulis, "Magnetic response of split-ring resonators in the far-infrared frequency regime," *Opt. Lett.* **30**, 1348-1350 (2005).
- [3] Xiang Zhang, "Optical Bulk Metamaterials," Plenary talk at the Nanometa 2009, The 2nd European Topical Meeting on Nanophotonics and Metamaterials 5 - 8 January, 2009, Seefeld, Tirol, Austria; J. Valentine, S. Zhang, T. Zentgraf, E. Ulin-Avila, D. A. Genov, G. Bartal and X. Zhang, "Three-dimensional optical metamaterial with a negative refractive index," *Nature* **455**, 376-378 (2008).
- [4] M. W. Klein, M. Wegener, N. Feth and S. Linden, "Experiments on second- and third-harmonic generation from magnetic metamaterials," *Opt. Express* **15**, 5238-5247 (2007); erratum:*ibid.*, **16**, 8055 (2008).
- [5] V. M. Agranovich, Y.R. Shen, R.H. Baughman, and A. A. Zakhidov, "Linear and nonlinear wave propagation in negative refraction metamaterials," *Phys. Rev. B* **69**, 165112(7) (2004).
- [6] I. V. Shadrin, A. A. Zharov, and Yu. S. Kivshar, "Second-harmonic generation in nonlinear left-handed metamaterials," *J. Opt. Soc. Am. B* **23**, 529-534 (2006).
- [7] A.K. Popov, V.V. Slabko, and V.M. Shalaev, "Second harmonic generation in left-handed metamaterials," *Laser Phys. Lett.* **3**, pp. 293-297 (2006).
- [8] A. K. Popov and V. M. Shalaev, "Negative-index metamaterials: second-harmonic generation, Manley-Rowe relations and parametric amplifications," *Appl. Phys. B* **84**, 131-137 (2006).
- [9] M. Scalora, G. D'Aguanno, M. Bloemer, M. Centini, N. Mattiucci, D. de Ceglia, and Yu. S. Kivshar, "Dynamics of short pulses and phase-matched second-harmonic generation in negative-index materials," *Opt. Express* **14**, 4746-4756 (2006).
- [10] A. K. Popov and V. M. Shalaev, "Compensating losses in negative-index metamaterials by optical parametric amplification," *Opt. Lett.* **31**, 2169-2171 (2006).
- [11] A. K. Popov, S. A. Myslivets, T. F. George, and V. M. Shalaev, "Four-wave mixing, quantum control, and compensating losses in doped negative-index photonic metamaterials," *Opt. Lett.* **32**, 3044-3046 (2007).
- [12] A. K. Popov, S. A. Myslivets, and V. M. Shalaev, "Resonant nonlinear optics of backward waves in negative-index metamaterials," *Appl. Phys. B* **94**, Feb. 13 (2009) (on-line).
- [13] A. K. Popov, S. A. Myslivets, and V. M. Shalaev, "Microscopic Mirrorless Negative-index Optical Parametric Oscillator," *Opt. Lett.* **34**, 1165-1167 (2009).
- [14] A. K. Popov and S. A. Myslivets, "Transformable broad-band transparency and amplification in negative-index films," *Appl. Phys. Lett.* **93**, 191117(3) (2008).
- [15] N. Lazarides and GP Tsironis, "Coupled nonlinear Schroedinger field equations for electromagnetic wave propagation in nonlinear left-handed materials," *Phys. Rev. E* **71**, 036614 2005

- [16] P. Tassin, L. Gelens, J. Danckaert, I. Veretennicoff, G. Van der Sande, P. Kockaert, and M. Tlidi, "Dissipative structures in left-handed material cavity optics," *Chaos* **17**, 037116(11) (2007)
- [17] P. Kockaert, P. Tassin, G. Van der Sande, I. Veretennicoff, and M. Tlidi, "Negative diffraction pattern dynamics in nonlinear cavities with left-handed materials," *Phys. Rev. A* **74**, 033822 (2006).
- [18] A. D. Boardman, N. King, R. C. Mitchell-Thomas, V. N. Malnev, Y. G. Rapoport, "Gain control and diffraction-managed solitons in metamaterials," *Metamaterials* **2**, 145-154 (2008)
- [19] G. D'Aguanno, N. Mattiucci, M. Scalora, and M. J. Bloemer, "Bright and Dark Gap Solitons in a Negative Index Fabry-Perot Etalon," *Phys. Rev. Lett.* **93**, 213902(1) (2004):
- [20] N. M. Litchinitser, I. R. Gabitov, A. I. Maimistov, and V. M. Shalaev, "Negative Refractive Index Metamaterials in Optics" (review paper), *Progress in Optics*, Editor Emil Wolf, Elsevier, **51**, Chapter 1, pp. 1-68 (2007); *ibid.*, "Effect of an optical negative index thin film on optical bistability," *Opt. Lett.* **32**, 151-153 (2007).
- [21] A.I. Maimistov and I.R. Gabitov, "Nonlinear optical effects in artificial materials," *Eur. Phys. J. Special Topics "Nonlinear Waves in Complex Systems: Energy Flow and Geometry"*, Editors Jean-Guy Caputo and Mads Peter Soerensen, Springer, **147**, 265-286 (2007).
- [22] S. E. Harris, "Proposed backward wave oscillations in the infrared," *Appl. Phys. Lett.* **9**, 114-117, 1966.
- [23] J. B. Khurgin, "Mirrorless magic," *Nat. Photonics* **1**, 446-447, 2007.
- [24] C. Canalias and V. Pasiskevicius, "Mirrorless optical parametric oscillator," *Nat. Photonics* **1**, 459-462, 2007.
- [25] K.I. Volyak, A.S. Gorshkov, "Investigations of a reverse-wave parametric oscillator," *Radiotekhnika i Elektronika (Radiotechnics and Electronics)* **18** 2075-2082, 1973 (Moscow, in Russian).
- [26] J. M. Manley and H. E. Rowe, "General energy relations in nonlinear reactances," *Proc. IRE* **47**, 2115-2116 (1959).
- [27] A. Yariv, *Quantum Electronics*, 2d ed., New York: Wiley, 1975, Ch. 18.
- [28] A. K. Popov, S. A. Myslivets, and T. F. George, "Nonlinear interference effects and all-optical switching in optically-dense inhomogeneously-broadened media," *Phys. Rev. A* **71**, 043811(13) (2005).

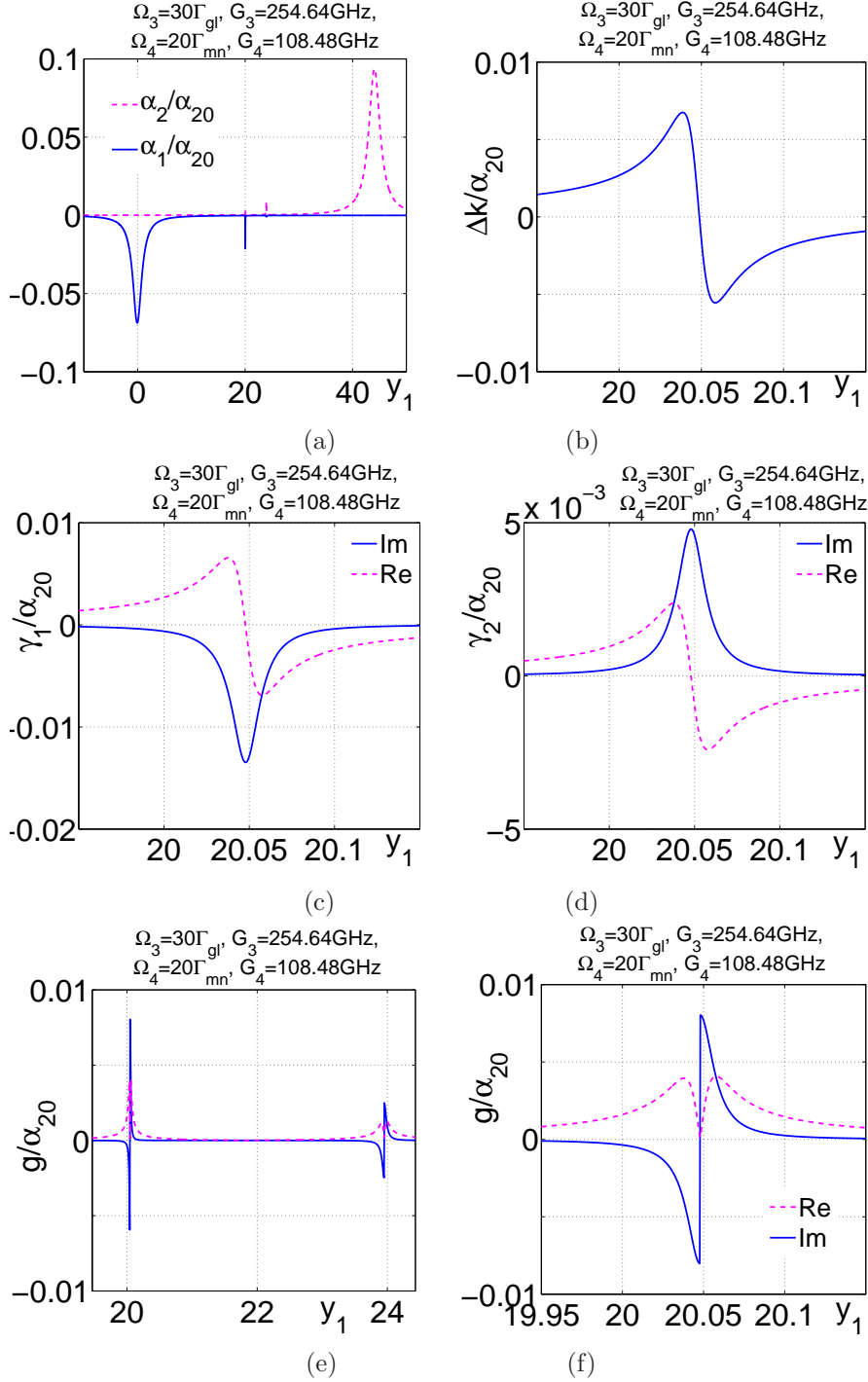


Figure 4. Nonlinear spectral structures in local optical quantities produced by the control fields. $y_1 = (\omega_1 - \omega_{gn})/\Gamma_{gn}$, $\omega_2 = \omega_3 + \omega_4 - \omega_1$. (a): absorption/gain indices for the signal and the idler; (b): phase mismatch; (c)-(f): four-wave mixing coupling parameters. Coupling Rabi frequencies and resonance frequency offsets for the control fields are: $G_3 = 254.64 \text{ GHz}$, $\Omega_3 = 30\Gamma_{gl}$, $G_4 = 108.48 \text{ GHz}$, $\Omega_4 = 20\Gamma_{mn}$.

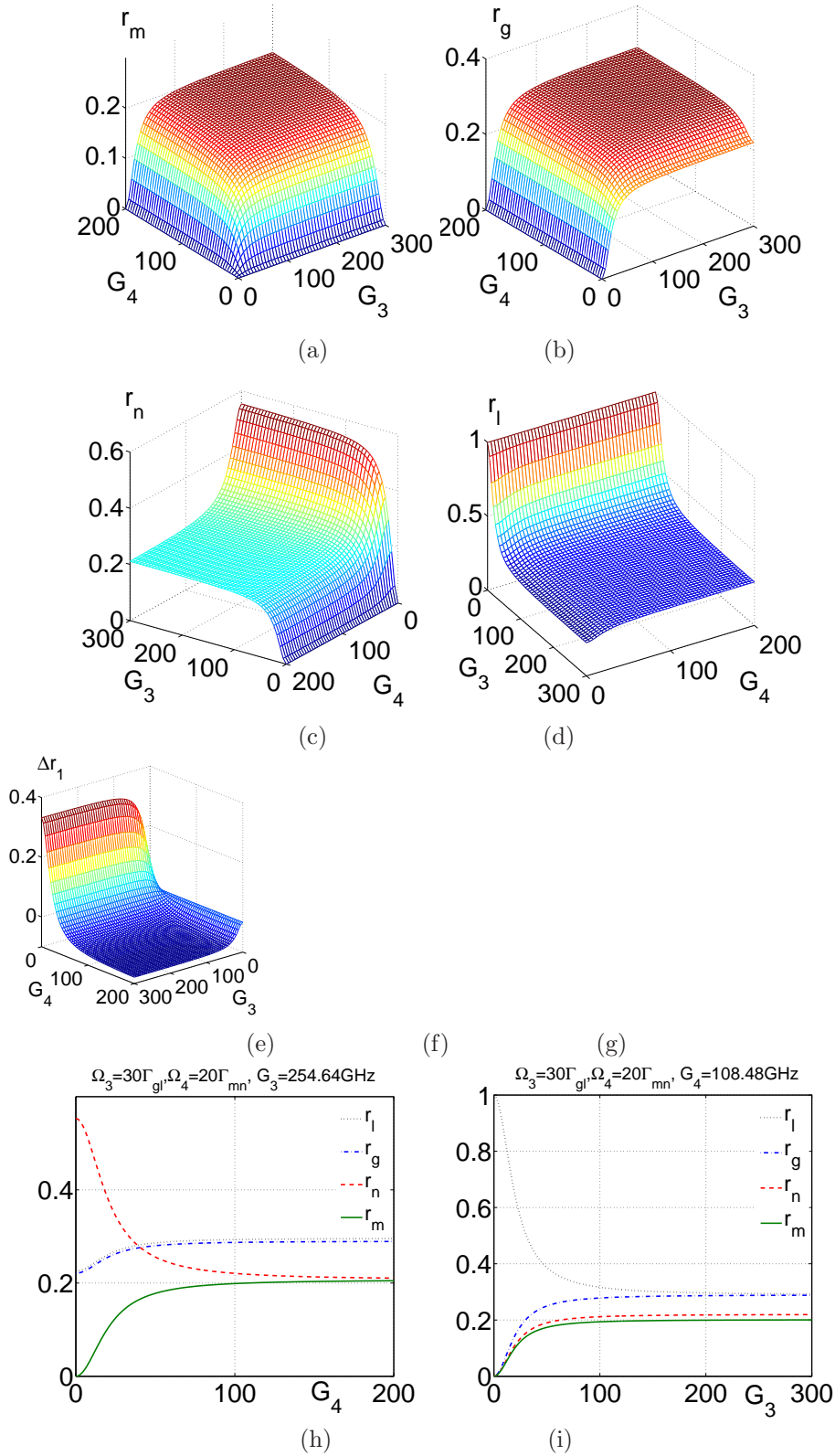


Figure 5. Difference of the energy-level populations and their dependence on the Rabi frequency of the control fields G_3 and G_4 (given in GHz). $\Omega_3 = 30\Gamma_{gl}$, $\Omega_4 = 20\Gamma_{mn}$. (h): $G_3 = 254.64$ GHz, (i): $G_4 = 108.48$ GHz.

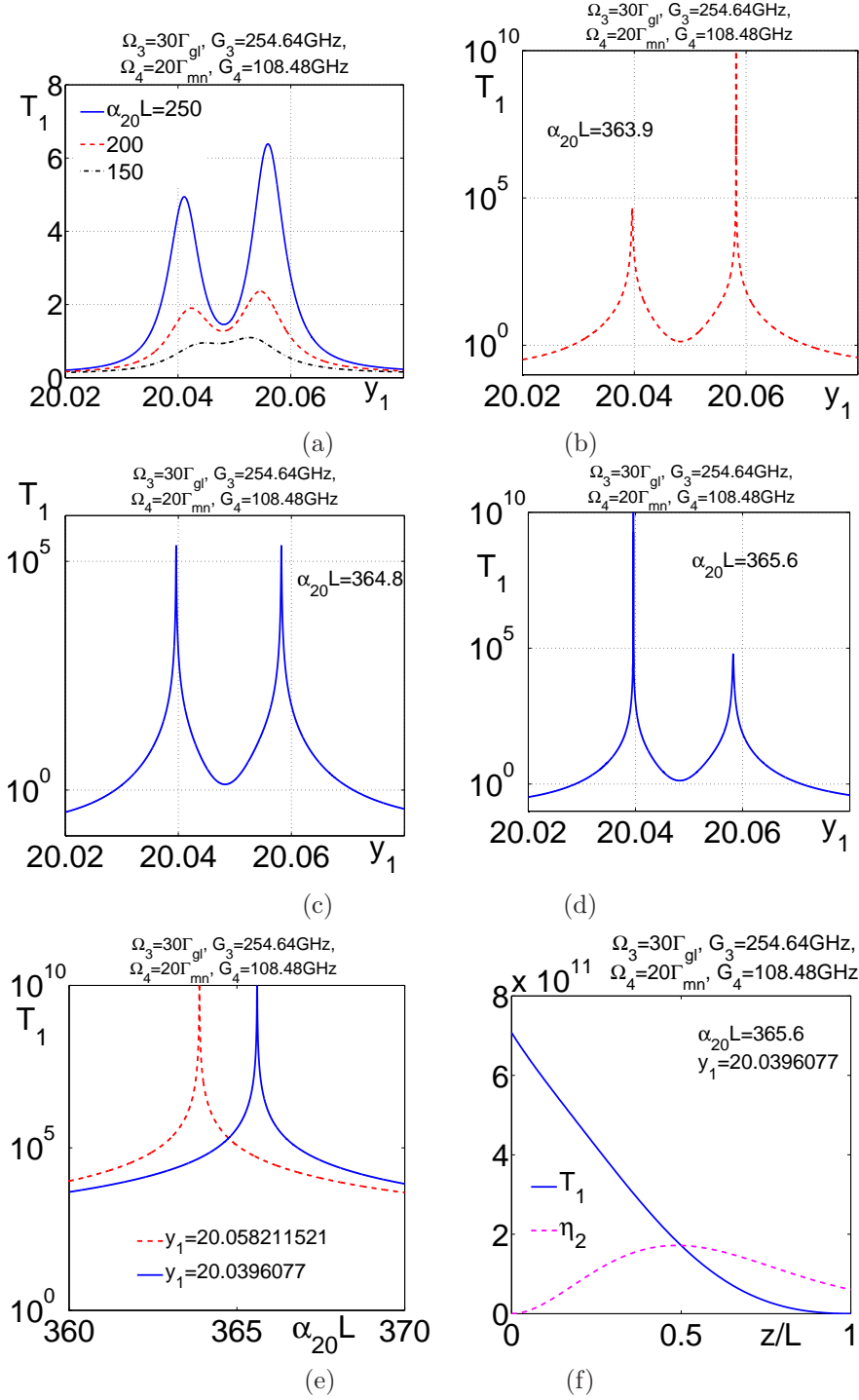


Figure 6. Dependence of the transmission of the slab on the resonance frequency offset $y_1 = (\omega_1 - \omega_{gn})/\Gamma_{gn}$ for different optical densities of the slab, (a)-(d), on the resonant optical density of the slab, (e), and the distribution of the signal and the idler along the slab, (f). $G_3 = 254.64\text{GHz}$, $\Omega_3 = 30\Gamma_{gl}$, $G_4 = 108.48\text{GHz}$, $\Omega_4 = 20\Gamma_{mn}$.

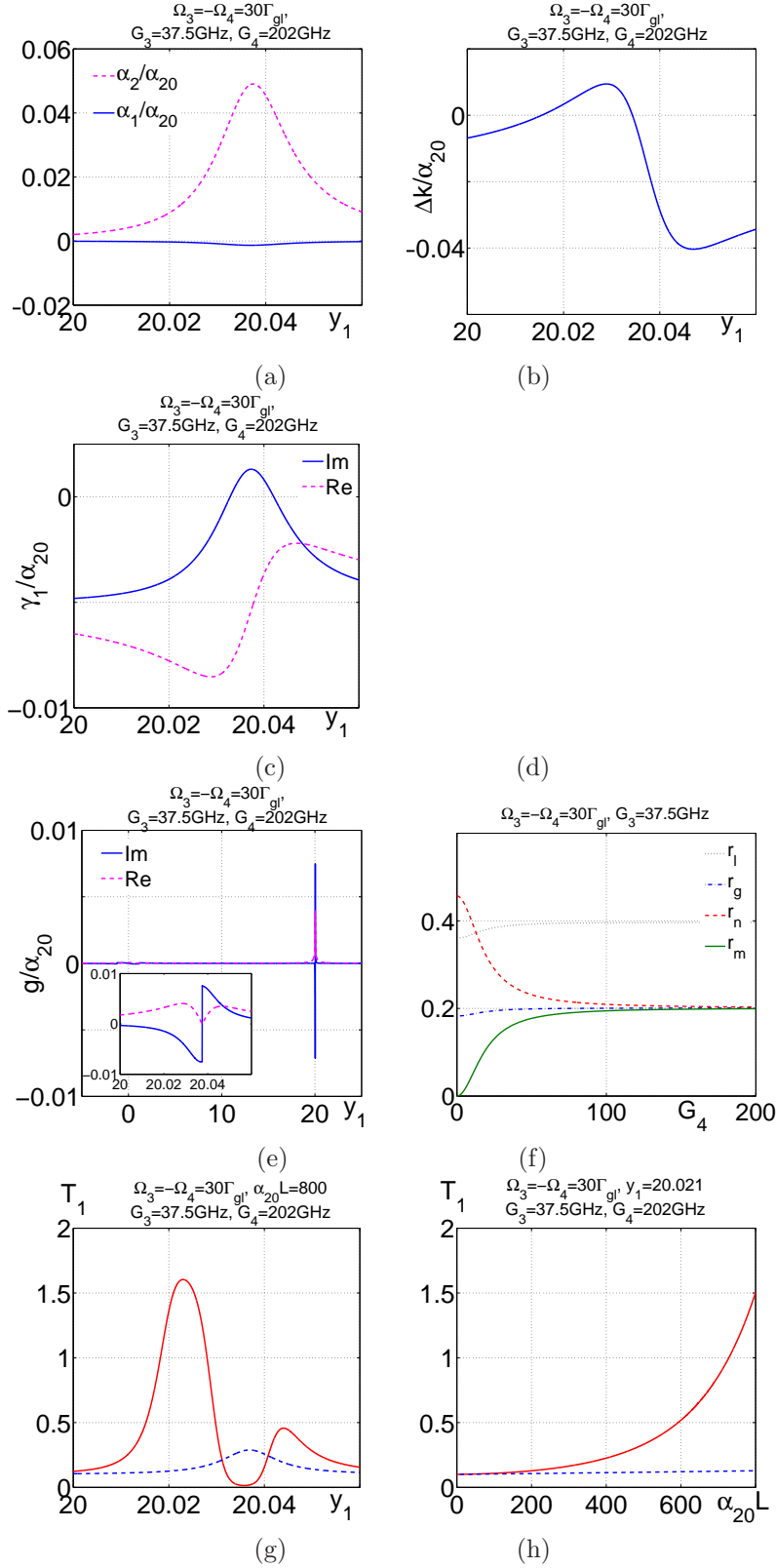


Figure 7. Energy-conversion in the scheme with neither population inversion nor two-photon gain possible [$\gamma_{mn} = 9 \times 10^7 \text{ sec}^{-1}$]; all other relaxation parameters are the same as in the previous case]. $y_1 = (\omega_1 - \omega_{gn})/\Gamma_{gn}$, $\omega_2 = \omega_3 + \omega_4 - \omega_1$. (a): absorption indices for the signal and the idler; (b): phase mismatch; (c)-(f): four-wave mixing coupling parameters; (g) and (h): transmission factor, the dashed line shows transmission at $g = 0$. Coupling Rabi frequencies and resonance frequency offsets for the control fields are: $G_3 = 37.5 \text{ GHz}$, $G_4 = 202 \text{ GHz}$, $\Omega_3 = -\Omega_4 = 30\Gamma_{gl}$.

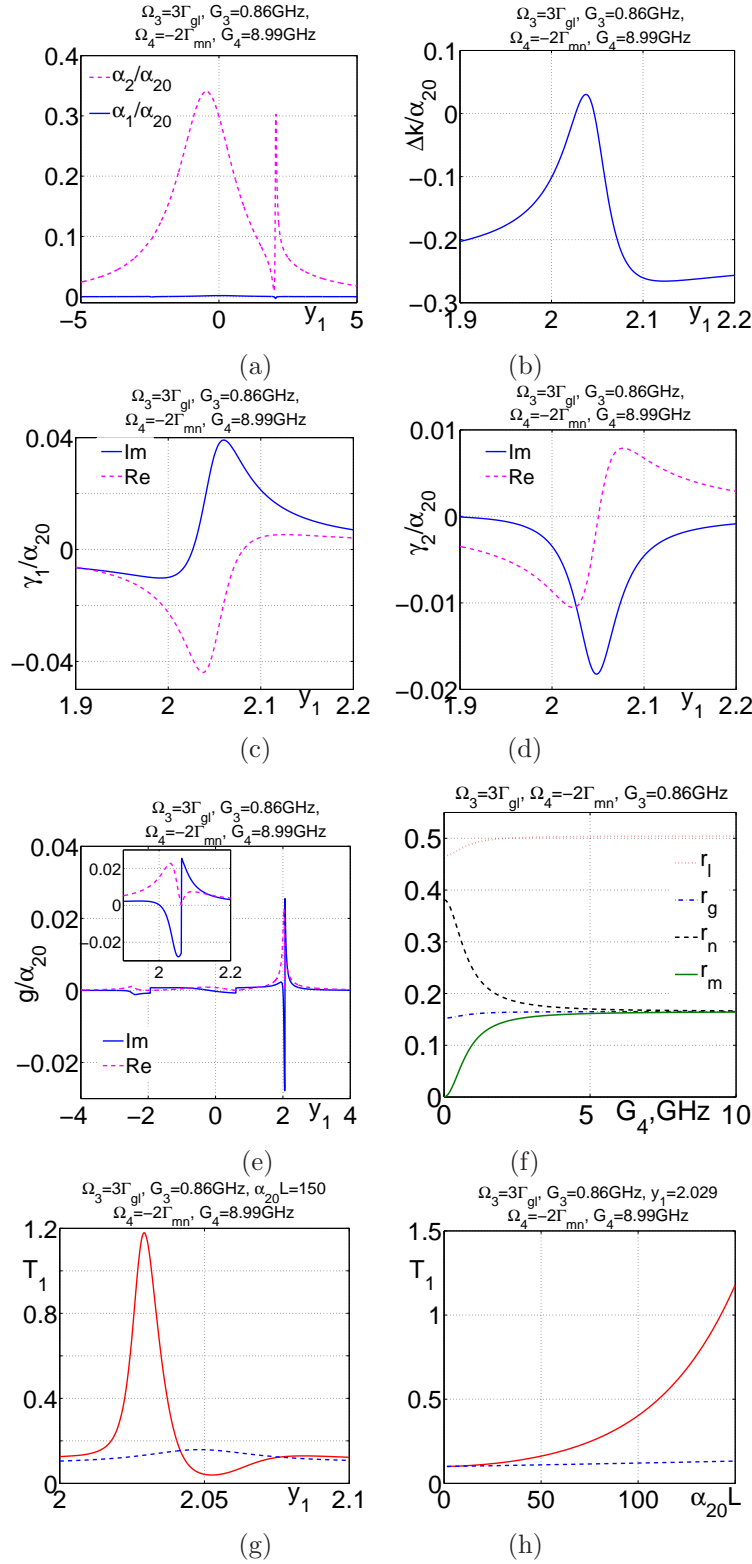


Figure 8. Quasi-resonant coupling at lower quantum coherence relaxation rates and at neither population inversion nor two-photon gain possible [$\Gamma_{gl}=1.8$, $\Gamma_{mn}=1.9$, $\Gamma_{gn}=1$, $\Gamma_{ml}=1.5$, $\Gamma_{mg} = 5 \times 10^{-2}$, $\Gamma_{nl} = 5 \times 10^{-3}$ (in 10^{11}sec^{-1}); all other relaxation parameters are the same as in the previous case]. $y_1 = (\omega_1 - \omega_{gn})/\Gamma_{gn}$, $\omega_2 = \omega_3 + \omega_4 - \omega_1$. (a): absorption indices for the signal and the idler; (b): phase mismatch; (c)-(e): four-wave mixing coupling parameters; (f): energy level populations; (g) and (h): transmission factor, dash line shows transmission at $g = 0$. Coupling Rabi frequencies and resonance frequency offsets for the control fields are: $G_3=0.86 \text{GHz}$, $\Omega_3 = 3\Gamma_{gl}$; $G_4=8.99 \text{GHz}$, $\Omega_4 = -2\Gamma_{mn}$.

